Spiral-wave Dynamics Depends Sensitively on Inhomogeneities in Mathematical Models of Ventricular Tissue

T K Shajahan[1], Sitabhra Sinha[2], and Rahul Pandit[1,3]

[1] *Centre for Condensed Matter Theory, Department of Physics,*
Indian Institute of Science, Bangalore 560012, INDIA

[2] *The Institute of Mathematical Sciences, C. I. T. Campus, Taramani, Chennai 600113, INDIA*

[3] *also at Jawaharlal Nehru Centre for Advanced Scientific Research, Bangalore 560064, INDIA*

Every sixth death in industrialized countries occurs because of cardiac arrhythmias like ventricular tachycardia (VT) and ventricular fibrillation (VF). There is growing consensus that VT is associated with an unbroken spiral wave of electrical activation on cardiac tissue but VF with broken waves, spiral turbulence, spatiotemporal chaos and rapid, irregular activation. Thus spiral-wave activity in cardiac tissue has been studied extensively. Nevertheless, many aspects of such spiral dynamics remain elusive because of the intrinsically high-dimensional nature of the cardiac-dynamical system. In particular, the role of tissue heterogeneities in the stability of cardiac spiral waves is still being investigated. Experiments with conduction inhomogeneities in cardiac tissue yield a variety of results: some suggest that conduction inhomogeneities can eliminate VF partially or completely, leading to VT or quiescence, but others show that VF is unaffected by obstacles. We propose theoretically that this variety of results is a natural manifestation of a complex, fractal-like boundary that must separate the basins of the attractors associated, respectively, with spiral breakup and single spiral wave. We substantiate this with extensive numerical studies of Panfilov and Luo-Rudy I models, where we show that the suppression of spiral breakup depends sensitively on the position, size, and nature of the inhomogeneity.

PACS numbers:

I. INTRODUCTION

The challenge of understanding the dynamics of spiral waves in excitable media is especially important in cardiac tissue where such waves are implicated in life-threatening arrhythmias such as ventricular tachycardia (VT) and ventricular fibrillation (VF)[1–7] . *Anatomical reentry* because of conduction inhomogeneities in cardiac tissue, and *functional reentry*[3], which result from wave propagation around transiently inexcitable regions, are crucial for the initiation of RS (a single rotating spiral wave) and the initiation and maintenance of ST (spiral turbulence with broken waves). But the precise ways in which spiral waves are affected by obstacles in ventricular tissue is still not clear[8]. Spiral waves form when waves of excitation circulate around an anatomical obstacle[9]. However, Allesie *et al* [10] have shown that spiral-wave formation can also occur with a functionally determined heterogeneity in the tissue. The interaction of such a wave with an anatomical obstacle can be quite complex especially in the spatiotemporally chaotic state associated with spiral turbulence. Indeed, experiments with obstacles in cardiac tissue have yielded a variety of results. For example, some experiments[11] report that small obstacles do not affect spiral waves but, as the size of the obstacle is increased, such a wave can get pinned to the obstacle. Various other experiments have discussed the role of an anatomical obstacle as an anchoring site for spiral waves, which can lead to the conversion of ST into RS [12–14]. Davidenko *et al* [15] have found that, when they induced spiral waves in cardiac tissue preparations "... in most episodes, the spiral was anchored to small

arteries or bands of connective tissue, and gave rise to stationary rotations. In some cases the core drifted away from its site of origin and dissipated at the tissue border." Other studies have shown [16–19] that an obstacle, in the path of a moving spiral wave, can break it and lead to many competing spiral waves. Recent experiments by Hwang *et al* [20] have suggested that multistability of spirals with different periods in the same cardiac-tissue preparation can arise because of the interaction of spiral tips with small-scale inhomogeneities.

Conduction inhomogeneities in the ventricle include scar tissues, resulting from an infarction, or major blood vessels. Some theoretical studies of the effects of tissue inhomogeneities have been carried out by using model equations for cardiac tissue; however, they have not addressed the issues we concentrate on. The interaction of an excitation wave with piecewise linear obstacles has been studied by Starobin *et al* [21] to understand the role of obstacle curvature in the pinning of such waves. Xie *et al* [22] have considered spiral waves around a circular obstacle and given a plausible connection of the ST-RS transition to the size of the obstacle. Panfilov *et al* [23–25] have shown that a high concentration of randomly distributed non-excitable cells can suppress spiral break up. Conduction inhomogeneities can also play a very important role in pacing termination of cardiac arrhythmias [26]; in particular, it is easier to remove a spiral wave once it is pinned to an obstacle, as described in Refs. [27, 28], than to control a state with spiral-turbulence.

Here we initiate a study that has been designed specifically to systematize the effects of conduction inhomogeneities in mathematical models for cardiac arrhyth-

mias. Our work shows clearly that ST can be suppressed or not suppressed by obstacles of different sizes depending on where they are placed. As we argue below, this *sensitive dependence* on the sizes and positions of obstacles must be a manifestation of a complex, fractal-like boundary [29, 30] between the domains of attraction of ST and RS. We also show that inhomogeneities in parameters, which govern ratios of time scales, lead to similar results. The models and numerical methods used by us is described in section II. Section III contains results; and we end with a discussion in Section IV.

II. MODELS AND NUMERICAL METHODS

We use the Panfilov [31, 32] and Luo-Rudy I [35, 36] models for cardiac tissue in our studies; the former is well suited for extensive numerical studies because of its relative simplicity; the latter, being realistic, allows us to check that the results we obtain are qualitatively correct and not artifacts of the Panfilov model.

The Panfilov model [31, 32] consists of two coupled equations, one a partial differential equation (PDE) and the other an ordinary differential equation (ODE), that specify the spatiotemporal evolution of the scaled transmembrane potential V (denoted by e in Refs. [31, 32]) and the recovery variable g, into which this model lumps all the effects of the different ion channels:

$$\partial V/\partial t = \nabla^2 V - f(V) - g;$$
$$\partial g/\partial t = \epsilon(V, g)(kV - g). \qquad (1)$$

The initiation of action potential is encoded in $f(V)$, which is piecewise linear: $f(V) = C_1 V$, for $V < e_1$, $f(V) = -C_2 V + a$, for $e_1 \leq V \leq e_2$, and $f(V) = C_3(V-1)$, for $V > e_2$. The physically appropriate parameters given in Refs. [31, 32] are $e_1 = 0.0026$, $e_2 = 0.837$, $C_1 = 20$, $C_2 = 3$, $C_3 = 15$, $a = 0.06$ and $k = 3$. The function $\epsilon(V, g)$ determines the dynamics of the recovery variable: $\epsilon(V, g) = \epsilon_1$ for $V < e_2$, $\epsilon(V, g) = \epsilon_2$ for $V > e_2$, and $\epsilon(V, g) = \epsilon_3$ for $V < e_1$ and $g < g_1$ with $g_1 = 1.8$, $\epsilon_1 = 0.01$, $\epsilon_2 = 1.0$, and $\epsilon_3 = 0.3$. As in Refs. [31, 32], we define dimensioned time T to be 5 ms times dimensionless time and 1 spatial unit to be 1 mm. The dimensioned value of the conductivity constant D is 2 cm^2/s.

In spite of its simplicity, relative to the Luo-Rudy I (LRI) model described below, the Panfilov model has been shown to capture several essential features of the spatiotemporal evolution of V in cardiac tissue [31–34]. As in the LR I model the Panfilov model also contains an absolute and a relative refractory period. The ways in which spiral patterns appear, propagate and break up, and the methods by which they can be controlled are very similar in these models. To make sure that the qualitative features we find are not artifacts of the Panfilov model we show explicitly, in illustrative cases, that they also occur in the realistic Luo-Rudy I model, which is based on the Hodgkin-Huxley formalism and takes into account the details of 6 ionic currents (e.g., Na$^+$, K$^+$, and Ca^{2+}) and 9 gate variables for the voltage-gated ion channels that regulate the flow of ions across the membrane [35]. The concentration difference of the ions, inside and outside the cell, induces a potential difference of approximately -84 mV across the cell membrane in the quiescent state. Stimuli, which raise the potential across the cell membrane above -60 mV, change the conductivity of the ion channels and yield an action potential that lasts typically for about 200 ms. Once an action potential is initiated there is a refractory period during which the same stimulus cannot lead to further excitation. Single cells in the Luo-Rudy model are coupled diffusively; thus one must solve a PDE for the transmembrane potential V; the time evolution and V dependence of the currents in this PDE are given by 7 coupled ordinary differential equations [35, 36] which we give in the Appendix.

We integrate the Panfilov model PDEs in d spatial dimensions by using the forward-Euler method in time t, with a time step $\delta t = 0.022$, and a finite-difference method in space, with step size $\delta x = 0.5$ and five-point and seven-point stencils, respectively, for the Laplacian in $d=2$ and $d=3$. Our spatial grids consist of square or simple-cubic lattices with side L mm, i.e., $(2L)^d$ grid points; we have used $L=200$. Similarly for the LRI model PDEs we use a forward-Euler method for time integration, with $\delta t = 0.01$ ms, a finite-difference method in space, with $\delta x = 0.0225$ cm, and a square simulation domain with 400×400 grid points, i.e., $L=90$ mm. We have checked in representative simulations on somewhat smaller domains that a Crank-Nicholson scheme yields results in agreement with the numerical scheme described above.

For both models we use no-flux (Neumann) boundary conditions on the edges of simulation domain and on the boundaries of obstacles. We introduce conduction inhomogeneities in the medium by setting the diffusion constant D equal to zero in regions with obstacles; in all other parts of the simulation domain D is a nonzero constant. The dimensioned value of D is 2 cm^2/s for the Panfilov model and between 0.5 cm^2/s and 1 cm^2/s for the LRI model; we use $D=0.5$ cm^2/s in the LRI simulations we report here . In most of our studies the inhomogeneity is taken to be a square region of side l , with 10 mm $\leq l \leq 40$ mm; however, we have also carried out illustrative simulations with circular or irregularly shaped inhomogeneities. In our three-dimensional simulations we use an obstacle of height 4 mm and a square base of side 40 mm, i.e., 8 and 80 grid points, respectively (For a detailed understanding of the three-dimensional case we must also consider the effects of rotational anisotropy of muscle fibers in cardiac tissue[37], but this lies outside the scope of our study.) We also study inhomogeneities in which ϵ_1 in model (1) varies over the simulation domain but D is constant.

The initial conditions we use are such that, in the absence of inhomogeneities, they lead to a state that displays spatiotemporal chaos and spiral turbulence. For
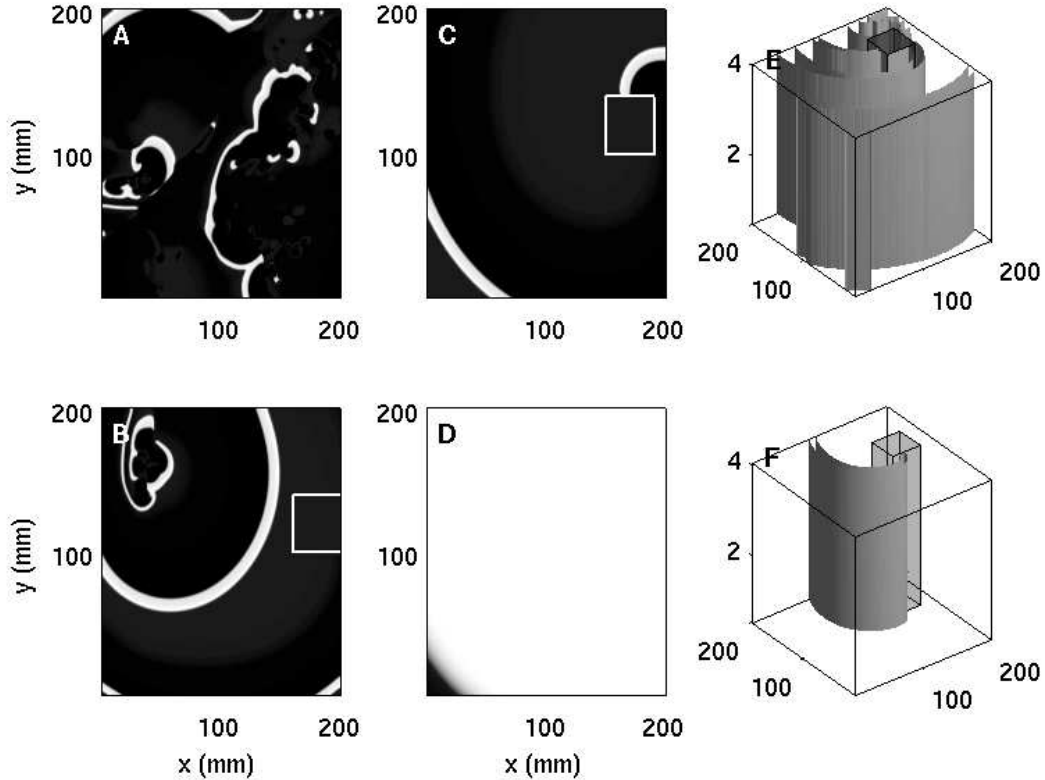
FIG. 1: **Panfilov-model spiral turbulence (ST)**: Transmembrane potentials for two dimension (pseudo-greyscale plots A-F) and three dimension (isosurface plots G and H). Two-dimensions:200 mm ×200 mm domain and a 40 mm × 40 mm square obstacle with left-bottom corner at (x, y). (**A**) no obstacle -ST; (**B**) $(x = 160, y = 100)$ ST persists; (**c**) $(x = 150, y = 100)$ ST replaced by RS (one rotating anchored spiral); (**D**) $(x = 140, y = 100)$ spiral moves away (medium quiescent). Three-dimensional analogs of (B) and (C): $(200 \times 200 \times 4)$ domain; an obstacle of height 4 mm and a square base of side 40 mm at (**E**) $(x = 140, y = 120, z = 0)$ and (**F**) $(x = 140, y = 110, z = 0)$.

the Panfilov model we start with a broken-wavefront initial condition: For a system of linear size L at time $t=0$ we set $g=2$, for $0 \leq x \leq L$ and $0 \leq y \leq \frac{L}{2}$, and $g = 0$ elsewhere, and $V = 0$ everywhere except for $y = \frac{L}{2} + 1$ and $0 \leq x \leq \frac{L}{2}$, where $V = 0.9$. From this broken wavefront a spiral wave develops with a core in the centre of the simulation domain and, in the absence of inhomogeneities, evolves to a state with broken spiral waves and turbulence (Fig. 1A). The spirals continue to break up even after 35000 ms for the parameters we use. For the LRI model we start from the initial condition shown in Fig. 2A which develops, without an obstacle, into the spiral-turbulent state shown in Fig. 2B.

In the presence of an obstacle the spiral turbulence (ST) state of Fig. 1A can either remain in the ST state or evolve into a quiescent state (Q) with no spirals or the RS state with one rotating spiral anchored at the obstacle. We explore all these possibilities in the next Section. Before we do so, we give the criteria we use to decide whether a given state, of the system we consider, is of type ST, RS, or Q. In the Panfilov model, if the spiral wave continue to form and break up even up to

3500 ms, we identify the state as ST (Fig. 1B); if, by contrast, a single spiral wave anchors to the obstacle and rotates around it at least for ten rotations ($\simeq 3500$ ms for the Panfilov model with a 40×40 mm^2 obstacle) we say that an RS state (Fig. 1C) has been achieved (we have seen that, once it anchors, this rotation of the spiral wave continues even after 100 rotation periods); lastly, if the spiral wave moves away from the simulation domain and is absorbed at the boundaries within 3500 ms, we conclude that the state is Q (Fig. 1D).

For the LRI model, if the spiral formation and break up continues upto 2200 ms, we identify the state as ST (Fig. 2C); if the spiral wave gets anchored to the obstacle and completes 4 rotation periods ($\simeq 2200$ ms for the obstacle we use) we identify the state as RS (Fig. 2D); and we say that the state Q (Figs. 2E and 2F) is achieved if the spiral wave moves away from the simulation domain within 2200 ms.
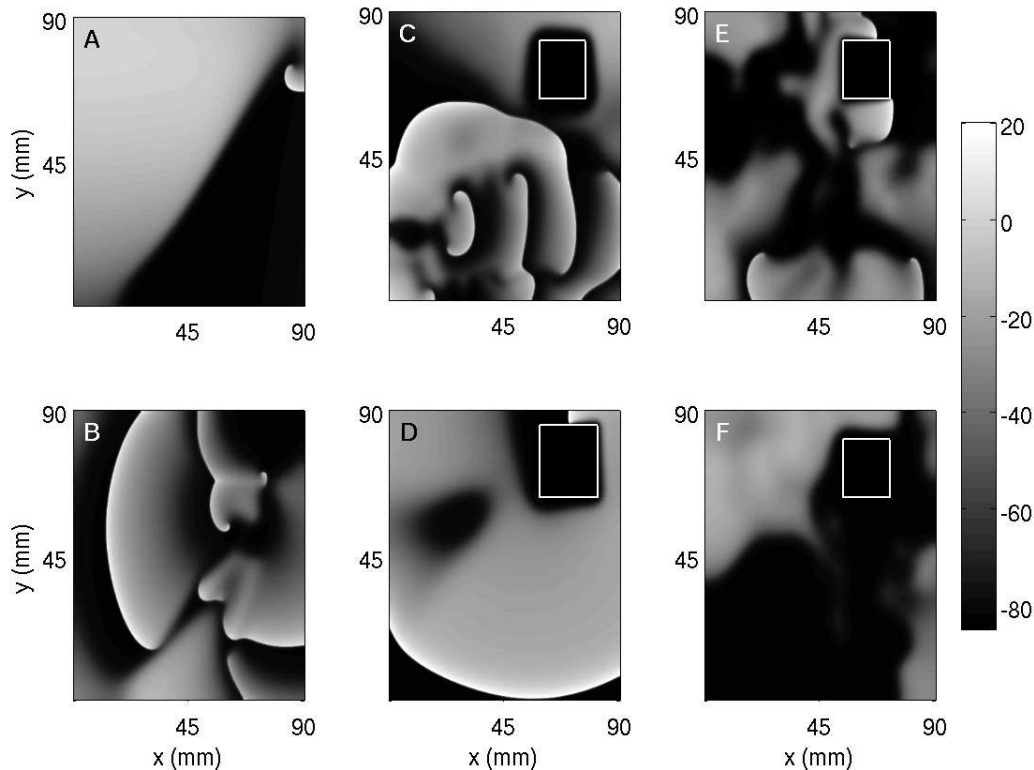
FIG. 2: **Luo-Rudy-Model spiral turbulence:** Pseudo-greyscale plots in a 90×90 mm^2 illustrating how the initial condition (**A**) evolves, in the absence of obstacles, to (**B**) via the generation of spiral waves and their subsequent breakup. In the presence of a square obstacle of side l placed with its bottom-left corner at (x, y) we obtain the following: (**C**)l=18 mm and ($x = 58.5$ mm, $y = 63$ mm) ST persists; (**D**)l=22.5 mm and ($x = 58.5$ mm, $y = 63$ mm) RS (one spiral anchored at the obstacle); for l=18 and ($x = 54$ mm,$y = 63$ mm) spirals disappear leaving the medium quiescent (**E**) at 800 ms and (**F**) at 1000 ms.

III. RESULTS

Cardiac tissue can have conduction inhomogeneities at various length scales. Even minute changes in cell or gap-junctional densities might act as conduction inhomogeneities[20]; these are of the order of microns. Scar tissues or blood vessels can lead to much bigger obstacles; these are in the mm to cm range so they can be studied effectively by using the PDEs mentioned above. Here we focus on such large obstacles. As in the experiments of Ikeda *et al* [11], we fix the position of the obstacle and study spiral-wave dynamics as a function of the obstacle size. For this we introduce a square obstacle of side l in the two-dimensional ($d = 2$) Panfilov model in a square simulation domain with side L=200 mm. We find that, with the bottom-left corner of the obstacle at the point (50 mm, 100 mm) spiral turbulence (ST) persists if $l \leq (40 - \Delta)$ mm, a quiescent state (Q) with no spirals is obtained if l= 40mm, and a state with a single rotating spiral (RS) anchored at the obstacle is obtained if $l \geq (40 + \Delta)$ mm. To obtain these results we have varied l from 2 to 80 mm in steps of Δ= 1 mm. Hence there is a clear transition from spiral turbulence to stable

spirals, with these two states separated by a state with no spirals.

The final state of the system depends not just on the size of the obstacle but also on how it is placed with respect to the tip of the initial wavefront. In our simulations we find, e.g., that even a small obstacle, placed close to the tip [l=10 mm obstacle placed at (100 mm, 100 mm)], can prevent the spiral from breaking up, whereas a bigger obstacle, placed far away from the tip [l= 75 mm, placed at (125 mm, 50 mm)], does not affect the spiral.

To understand in detail how the position of the obstacle changes the final state, we now present the results of our extensive simulations for the $d = 2$ Panfilov model in a square domain with side 200 mm, i.e., 400×400 grid points, and with a square obstacle of side l=40 mm. Figure 3A shows our simulation domain divided into small squares of side l_p mm (l_p=10 mm in Fig. 3A). The color of each small square indicates the final state of the system when the position of the lower-left corner of the obstacle coincides with that of the small square: white, black, and gray indicate, respectively, ST, RS, and Q. In Figs. 3B and 3C we show the rich, fractal-like structure of the interfaces between the ST, RS, and Q regions by zooming in successively on small subdomains encompassing sections
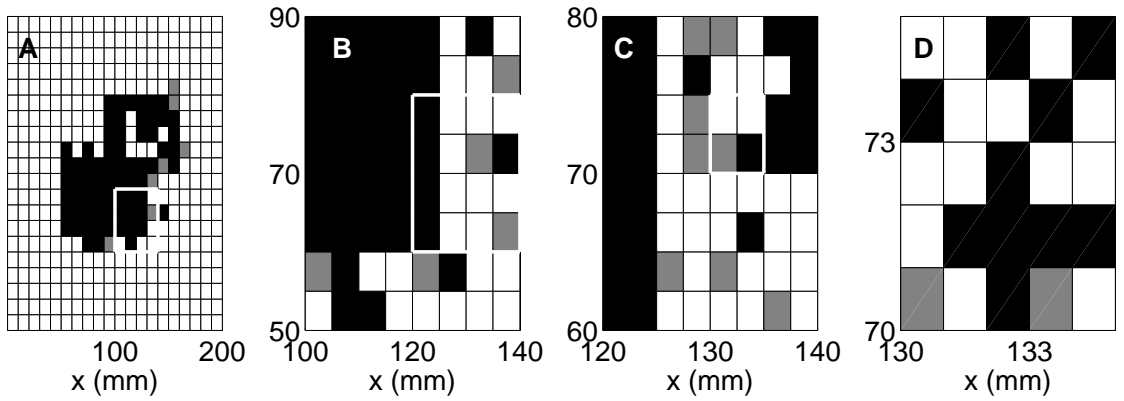
FIG. 3: **Panfilov-model stability diagram:** The effect of an 40×40 mm^2 obstacle in a 200×200 mm^2 domain shown by small squares (side l_p) the colors of which indicate the final state of the system when the position of the bottom-left corner of the obstacle coincides with that of the small square (white, black, and gray denote ST, RS, and Q, respectively). (**A**) for l_p=10 mm. We get the fractal-like structure of the interfaces between ST, RS, and Q by zooming in on small sub domains encompassing parts of these interfaces (white boundaries in **A**, **B**, and **C** with (**B**) l_p=5 mm, (**C**) l_p=2.5 mm, and (**D**) l_p= 1 mm).

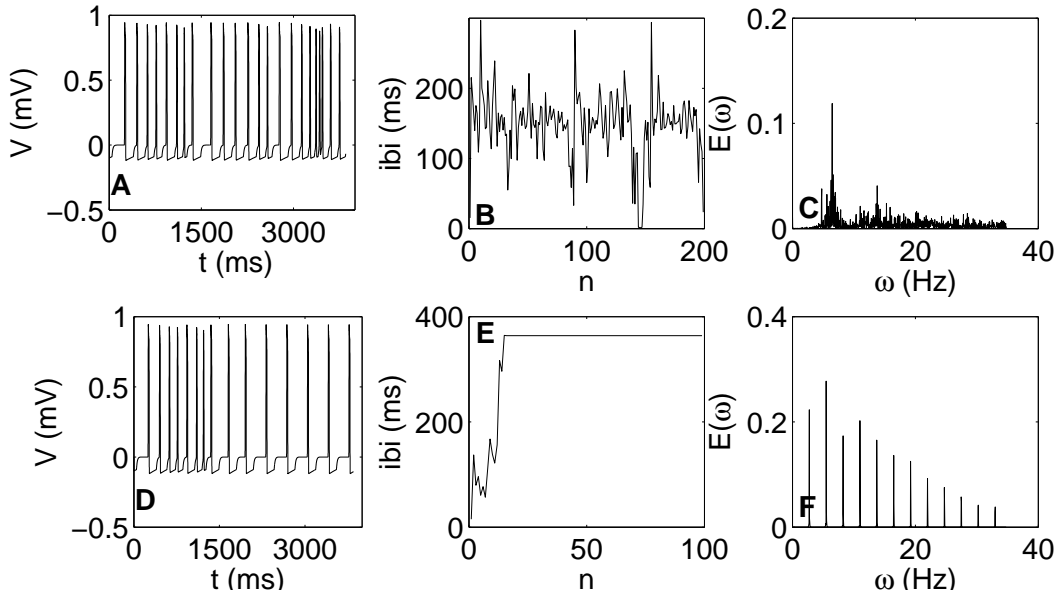FIG. 4: The local time series, interbeat interval IBI, and power spectrum of the transmembrane potential $V(x,y,t)$ at a representative point (x,y) in the tissue. When the obstacle is at (160 mm,100 mm) a spiral turbulent state ST is obtained with the time series (**A**), and interbeat interval (**B**)showing non-periodic chaotic behavior and a broad-band power spectrum (**C**). However, with the bottom-left corner of the obstacle at (150 mm,100 mm), the spiral wave gets attached to the obstacle after 9 rotations ($\simeq$ 1800 ms); this is reflected in the time series (**D**) and the plot of the interbeat interval(**E**); after transients the latter settles on to a constant value of 363 ms; the power spectrum (**F**) shows discrete peaks with a fundamental frequency ω_f = 2.74 Hz and its harmonics. Initial transients over the first 50,000 δt were removed before we collected data for calculating the power spectrum.

of these interfaces (white boundaries in Figs. 3A and 3B) and reducing the sizes of the small squares into which we divide the subdomain. Clearly very small changes in the position of the obstacle can change the state of the system from ST to Q or RS, i.e., the spatiotemporal evolution of the transmembrane potential depends very sensitively on the position of the obstacle.

The time series of the transmembrane potential $V(x,y,t)$ taken from a representative point (x,y) in the simulation domain illustrates the changes that occur when one moves from the ST to the RS regime in Fig. 3. Such time series are shown in Fig. 4. For example, when the obstacle is placed with its bottom-left corner at (160 mm, 100 mm), the system is in the spiral-
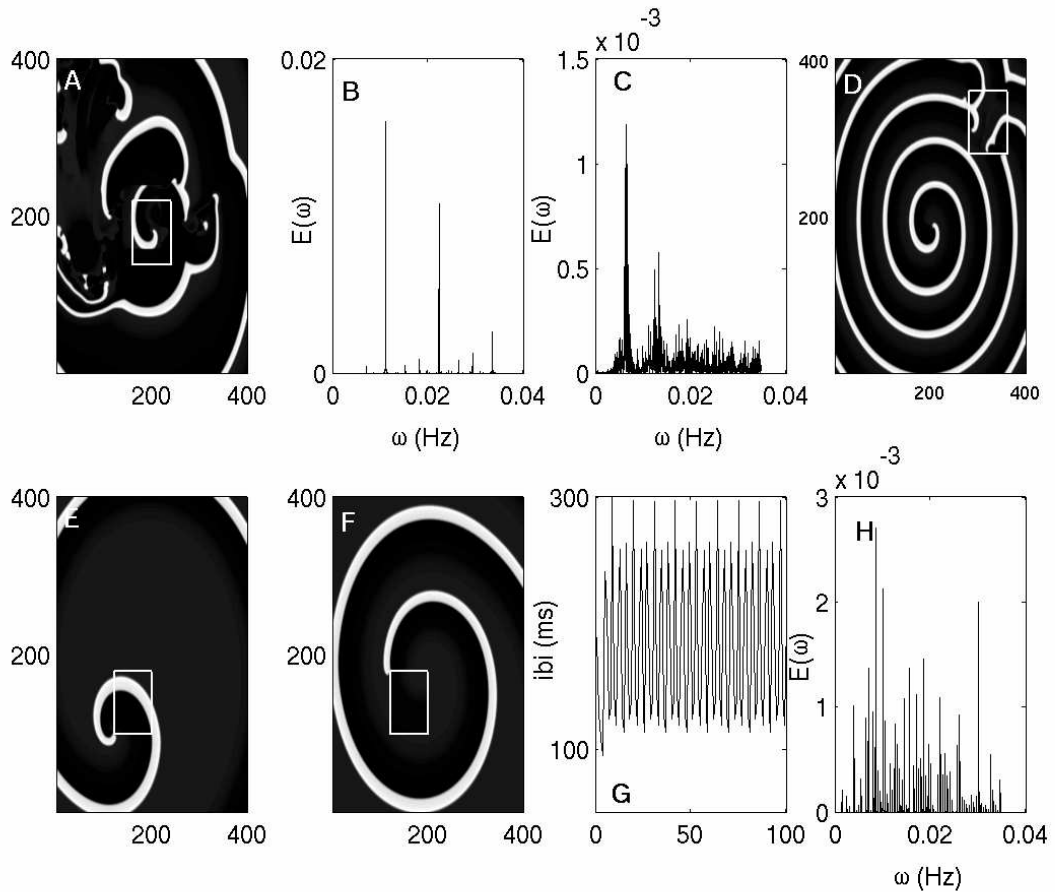
FIG. 5: **Inhomogeneities in ϵ_1 :** Inhomogeneities in the parameter ϵ_1 result in the coexistence of different types of spatiotemporal behavior in the same system. With ϵ_1^{out}=0.01 and ϵ_1^{in}=0.02 (see text), we obtain spatiotemporal chaos outside the inhomogeneity but quasiperiodic behavior inside it (**A**); the latter is illustrated by the power spectrum of $V(x,y,t)$ with discrete peaks (**B**) and the former by a broad-band power spectrum (**C**). With ϵ_1^{out}=0.03 and ϵ_1^{in}=0.01 and the left-bottom corner of the inhomogeneity placed at (x=140 mm, y=140 mm), single and broken spiral waves coexist in same medium (**D**), whereas, with the inhomogeneity at (x=60 mm, y=50 mm), a single rotating spiral gets anchored to the inhomogeneity (**E, F**) with quasiperiodic behavior illustrated by the interbeat interval (**G**) and the power spectrum (**H**). The power spectrum (**H**) shows six frequencies ($\omega_1 = 4.06, \omega_2 = 5.56, \omega_3 = 6.57, \omega_4 = 7.05, \omega_5 = 8.58$, and $\omega_6 = 9.07$ Hz) not rationally related to each other; all other frequencies can be expressed as $\sum_{i=1}^{6} n_i\omega_i$, where the n_i are integers. Initial transients over the first 50,000 δt were removed before we collected data for calculating power spectra.

turbulent state ST. The time series of V from the point (51 mm, 50 mm) clearly shows non periodic, chaotic behavior. The times between successive spikes in such time series, or interbeat intervals (IBI), are plotted versus the integers n, which label the spikes, in Fig. 4B; this also shows the chaotic nature of the state ST. Figure 4C shows the power spectrum $E(\omega)$ of the time series in Fig. 4A; the broad-band nature of this power spectrum provides additional evidence for the chaotic character of ST. By combining Figs. 4A-4C with the pseudo-greyscale plots of Figs. 1A and 1B we conclude that ST is not merely chaotic but exhibits *spatiotemporal chaos*. Indeed, it has been shown that the Panfilov model, in the spiral turbulence regime, has several positive Lyapunov exponents whose number increases with the size of the simulation domain; consequently the Kaplan-Yorke dimension also

increases with the system size (see Fig.4 of Ref.[33]); this is a clear indication of spatiotemporal chaos.

If we change the position of the obstacle slightly and move it such that its left-bottom corner is at the position (150 mm, 100 mm), the spiral eventually gets attached to the obstacle. For this case the analogs of Figs. 4A-4C are shown, respectively, in Figs. 4D-4F. From the time series of Fig. 4D we see that the transmembrane potential displays some transients up to about 2000 ms but then it settles into periodic behavior. This is also mirrored in the plot of IBI versus n in Fig. 4E in which the transients asymptote to a constant value for the IBI (363 ms) which is characteristic of periodic spikes. Not surprisingly, the corresponding power spectrum in Fig. 4F consists of discrete spikes at frequencies $\omega_m = m\omega_f$, where m is a positive integer and ω_f is the fundamen-

tal frequency ($\omega_f = 2.74$ Hz). A simple rotating spiral anchored at the obstacle (Fig. 1C) will clearly result in such a periodic time series in the state RS.

We do not show the analogs of Figs. 4A-4C for the quiescent state Q since the transmembrane potential V just goes to zero after an initial period of transients. The durations for which the transients last, say in Fig. 4D, vary greatly depending on the position of the obstacle relative to the spiral tip. We have seen transient times ranging from 300 ms to 2000 ms in our simulations.

We obtain similar results for the three-dimensional Panfilov and the two-dimensional Luo-Rudy I models: Illustrative pictures from our simulations of spiral turbulence (ST) and a single rotating spiral (RS) anchored at the obstacle are shown in Figs. 1 and 2, respectively. From these and similar figures we note that the final state, ST, RS, or Q, depends not only on the size of the obstacle but also on its position. Obstacles of different shapes, e.g., circles, irregular shapes, and two squares separated from each other, lead to similar results (see `www.physics.iisc.ernet.in/~rahul/movies.html` for representative movies of our simulations).

We have also explored the effects inhomogeneities in parameters such as ϵ_1 in Eq. (1). In the Panfilov model, ϵ_1^{-1} is the recovery time-constant for large values of g and intermediate values of V[32]. As ϵ_1 increases the absolute refractory period of the action potential decreases and this in turn decreases the pitch of the spiral wave (cf. Fig.3 in Ref.[33]).

In a homogeneous simulation domain (of size say 200 × 200 mm^2) values of $\epsilon_1 > 0.03$ produce a single periodically rotating spiral. As ϵ_1 is lowered, e.g., if $\epsilon_1 < 0.02$, quasiperiodic behavior is seen; this is associated with the meandering of the tip of a simple rotating spiral. Even lower values of ϵ_1, say $\epsilon_1 = 0.01$ that we have used above, lead to spatiotemporal chaos. We now consider an inhomogeneous simulation domain in which all parameters in the model except ϵ_1 remain constant over the whole simulation domain. We then introduce a square inhomogeneity inside which ϵ_1 assumes the value ϵ_1^{in} and outside which it has the value ϵ_1^{out}. Different choices of ϵ_1^{in} and ϵ_1^{out} lead to the interesting behaviors we summarize below.

With a square patch of size 40 × 40 mm^2, $\epsilon_1^{in} = 0.02$, and $\epsilon_1^{out} = 0.01$, a spatiotemporally chaotic state is obtained for most positions of this inhomogeneity. But there are certain critical positions of this inhomogeneity for which all spirals are completely eliminated (e.g., when the left-bottom corner of the inhomogeneity is at x=70 mm, y=120 mm the spiral moves out of the simulation domain). For yet other positions of the inhomogeneity, spatiotemporal chaos is obtained outside the inhomogeneity but inside it quasiperiodic behavior is seen (Figs. 5A-5C). However, with $\epsilon_1^{in} = 0.01$ and $\epsilon_1^{out} = 0.03$, spiral breakup occurs inside the inhomogeneity and coexists with unbroken periodic spiral waves outside it (Fig. 5D), as previously noted by Xie *et al* [38]. Even in this case, for certain positions of the inhomogeneity, a single

spiral wave gets anchored to it (Figs. 5E, 5F) as in the case of a conduction inhomogeneity (Fig. 1C). However, the temporal evolution of V at a representative point in Fig. 5E is richer than it is in Fig. 1C: $V(x, y, t)$, with x=51 and y=50, displays the interbeat interval of Fig. 5G; the associated power spectrum shows six fundamental frequencies, not rationally related to each other, and their combinations; this indicates strong quasiperiodicity of $V(x, y, t)$. So, even an inhomogeneity in the excitability of the medium can cause the ST-RS or ST-Q transitions we have discussed above for the case of conduction inhomogeneities. Furthermore, an inhomogeneity in excitability can also lead to rich temporal behaviors as shown in Figs. 5 E-H.

IV. DISCUSSION

We have shown that spiral turbulence in models of cardiac arrhythmias depends sensitively on the size and position of inhomogeneities in the medium. In particular, we have shown that, with the inhomogeneity at a particular position, the state of the spiral wave changes from ST to RS as the size of the obstacle increases. We have also shown that, for an obstacle with fixed size, this transition also depend upon the position of the obstacle. Two important questions arise from our work: (1) What causes the sensitive dependence of such spiral turbulence on the positions and sizes of conduction inhomogeneities? (2) What are the implications of our theoretical study for cardiac arrhythmias and their control? We discuss both these questions below.

Spiral turbulence (ST) and a single rotating spiral (RS) in our models are like VF and VT, respectively, in cardiac tissue. Our study suggests, therefore, that such cardiac arrhythmias, like their ST and RS analogs in the Panfilov and Luo-Rudy I models, must depend sensitively on the positions and sizes of conduction inhomogeneities. Furthermore, our work indicates that this is a natural consequence of the spatiotemporal chaos associated with spiral turbulence [33, 39] in these models: Even for much simpler, low-dimensional dynamical systems it is often the case that a *fractal* basin boundary [29, 30] separates the basin of attraction of a strange attractor from the basin of attraction of a fixed point or limit cycle; thus a small change in the initial condition can lead either to chaos, associated with the strange attractor, or to the simple dynamical behaviors associated with fixed points or limit cycles.

The PDEs we consider here are infinite-dimensional dynamical systems; the complete basin boundaries for these are not easy to determine; however, it is reasonable to assume that a complex, fractal-like boundary separate the basins of attraction of spatiotemporally chaotic states (e.g., ST) and those with simpler behaviors (e.g., RS or Q). Here we do not change the initial condition; instead we change the dynamical system slightly by moving the position, size, or shape of a conduction inhomogeneity.

This too affects the long-time evolution of the system as sensitively as does a change in the initial conditions.

In particular, our work elucidates that, by changing the position of a conduction inhomogeneity, we may convert spiral breakup to single rotating spiral or vice versa as depicted graphically in Figs. 3 and 4. Even more exciting is the possibility that, at the boundary between these two types of behavior (Fig. 3), we can find the quiescent state Q. Thus our model study obtains all the analogs of possible qualitative behaviors found in experiments, namely, (1) ST might persist even in the presence of an obstacle, (2) it might be suppressed partially and become RS, or (3) it might be eliminated completely.

Our work on inhomogeneities in the parameter ϵ_1 in the Panfilov model illustrates the complex way in which the spatiotemporal evolution of the transmembrane potential depends on the properties of this model for cardiac tissue.

The implications of our results for anti-tachycardia-pacing and defibrillation algorithms, used for the suppression of cardiac arrhythmias, are very important. Optimal pacing algorithms might well have to be tailor made for different inhomogeneities. Indeed, clinicians often adapt their hospital procedures for the treatment of arrhythmias, on a case-by-case basis, to account for cardiac structural variations between patients [40]. We hope, therefore, that our work will stimulate further systematic experiments on the effects of obstacles on cardiac arrhythmias.

APPENDIX: THE LUO-RUDY MODEL

In the Luo-Rudy I (LR I) model there are six components of the ionic current, which are formulated mathematically in terms of Hodgkin-Huxley-type equations[41]. The partial differential equation for the transmembrane potential V is

$$\frac{\partial V}{\partial t} + \frac{I_{LR}}{C} = D\nabla^2 V. \qquad (A.1)$$

Here I_{LR} is the instantaneous, total ionic-current density. The subscript LR denotes that we use the formulation of the total ionic current described by the Luo-Rudy Phase I (LR1) model [35], where $I_{LR} = I_{Na} + I_{si} + I_K + I_{K1} + I_{Kp} + I_b$, with the current densities I_{Na} (fast inward Na^+), I_{si} (slow inward), I_K (slow outward *time-dependent* K^+), I_{K_1} (*time-independent* K^+), I_{Kp}

(plateau K^+), I_b (total background), given by:

$$
\begin{aligned}
I_{Na} &= G_{Na}m^3hj(V - E_{Na}); \\
I_{si} &= G_{si}df(V - E_{si}); \\
I_K &= G_K xx_i(V - E_K); \\
I_{K_1} &= G_{K_1}K_{1\infty}(V - E_{K_1}); \\
I_{Kp} &= G_{Kp}K_p(V - E_{Kp}); \\
I_b &= 0.03921(V + 59.87);
\end{aligned}
$$

and $K_{1\infty}$ is the steady-state value of the gating variable K_1. All current densities are in units of $\mu A/cm^2$, voltages are in mV, and G_ξ and E_ξ are, respectively, the ion-channel conductance and reversal potential for the channel ξ. The ionic currents are determined by the time-dependent ion-channel gating variables h, j, m, d, f, x, x_i, K_p and K_1 generically denoted by ξ, which follow ordinary differential equations of the type

$$\frac{d\xi}{dt} = \frac{\xi_\infty - \xi}{\tau_\xi},$$

where $\xi_\infty = \alpha_\xi/(\alpha_\xi + \beta_\xi)$ is the steady-state value of ξ and $\tau_\xi = \frac{1}{\alpha_\xi + \beta_\xi}$ is its time constant. The voltage-dependent rate constants, α_ξ and β_ξ, are given by the following empirical equations:

$$
\begin{aligned}
\alpha_h &= 0, \text{ if } V \geq -40 \text{ mV}, \\
&= 0.135 \ \exp{[-0.147 \ (V + 80)]}, \text{ otherwise}; \\
\beta_h &= \frac{1}{0.13 \ (1 + \exp{[-0.09(V + 10.66)]})}, \text{ if } V \geq -40 \text{ mV}, \\
&= 3.56 \ \exp{[0.079 \ V]} + 3.1 \times 10^5 \ \exp{[0.35 \ V]}, \text{ otherwise};
\end{aligned}
$$

$$
\begin{aligned}
\alpha_j &= 0, \text{ if } V \geq -40 \text{ mV}, \\
&= \left[\frac{(\exp{[0.2444 \ V]} + 2.732 \times 10^{-10} \ \exp{[-0.04391 \ V]})}{-7.865 \times 10^{-6}\{1 + \exp{[0.311 \ (V + 79.23)]}\}}\right] \\
&\quad \times (V + 37.78), \text{ otherwise}; \\
\beta_j &= \frac{0.3 \ \exp{[-2.535 \times 10^{-7} \ V]}}{1 + \exp{[-0.1 \ (V + 32)]}}, \text{if } V \geq -40 \text{ mV}, \\
&= \frac{0.1212 \ \exp{[-0.01052 \ V]}}{1 + \exp{[-0.1378 \ (V + 40.14)]}}, \text{ otherwise};
\end{aligned}
$$

$$
\begin{aligned}
\alpha_m &= \frac{0.32 \ (V + 47.13)}{1 - \exp{[-0.1 \ (V + 47.13)]}}; \\
\beta_m &= 0.08 \ \exp{[-0.0909 \ V]};
\end{aligned}
$$

$$
\begin{aligned}
\alpha_d &= \frac{0.095 \ \exp{[-0.01 \ (V - 5)]}}{1 + \exp{[-0.072 \ (V - 5)]}}; \\
\beta_d &= \frac{0.07 \ \exp{[-0.017 \ (V + 44)]}}{1 + \exp{[0.05 \ (V + 44)]}};
\end{aligned}
$$

$$\alpha_f = \frac{0.012 \ \exp\left[-0.008 \ (V+28)\right]}{1+\exp\left[0.15 \ (V+28)\right]};$$

$$\beta_f = \frac{0.0065 \ \exp\left[-0.02 \ (V+30)\right]}{1+\exp\left[-0.2 \ (V+30)\right]};$$

$$\alpha_x = \frac{0.0005 \ \exp\left[0.083 \ (V+50)\right]}{1+\exp\left[0.057 \ (V+50)\right]};$$

$$\beta_x = \frac{0.0013 \ \exp\left[-0.06 \ (V+20)\right]}{1+\exp\left[-0.04 \ (V+20)\right]};$$

$$\alpha_{K1} = \frac{1.02}{1+\exp\left[0.2385 \ (V-E_{K1}-59.215)\right]};$$

$$\beta_{K1} = \frac{\left[0.49124 \ \exp\left[0.08032 \ (V-E_{K1}+5.476)\right]\right.}{1+\exp\left[-0.5143 \ (V-E_{K1}+4.753)\right]}$$
$$\left. +\exp\left[0.06175 \ (V-E_{K1}-594.31]\right].\right.$$

The gating variables x_i and K_p are given by

$$x_i = \frac{2.837 \ \exp 0.04(V+77)-1}{(V+77)\exp 0.04 \ (V+35)}, \text{if } V > -100\text{mV},$$
$$= 1, \text{ otherwise};\tag{A.2}$$

$$K_p = \frac{1}{1+\exp\left[0.1672 \ (7.488-V)\right]}.\tag{A.3}$$

The values of the channel conductances G_{Na}, G_{si}, G_K, G_{K_1}, and G_{Kp} are 23, 0.07, 0.705, 0.6047 and 0.0183 mS/cm^2, respectively[42]. The reversal potentials are $E_{Na} = 54.4$ mV, $E_K = -77$ mV, $E_{K1} = E_{Kp} = -87.26$ mV, $E_b = -59.87$ mV, and $E_{si} = 7.7 - 13.0287 \ln Ca$, where Ca is the calcium ionic concentration satisfying

$$\frac{dCa}{dt} = -10^{-4}I_{si} + 0.07(10^{-4}-Ca).$$

The times t and τ_ξ are in ms; the rate constants α_ξ and β_ξ are in ms^{-1}.

---

[1] M. C. Cross, and P. C. Hohenberg, Rev. Mod. Phys. **65**, 851-1112 (1993).
[2] A. T. Winfree, Chaos **8**,1-19 (1998).
[3] J. Jalife, R. A. Gray, G. E. Morley, and J. M. Davidenko, Chaos **8**, 57-64 (1998).
[4] R. A. Gray, , J. Jalife, A. Panfilov, W. J. Baxter, J. M. Davidenko, and A. M. Pertsov, Science **270**, 1222-1223 (1995).
[5] F. X. Witkowski, L. J. Leon, P. A. Penkoske, W. R. Giles, M. L. Spano, W.L. Ditto, and A.T. Winfree, Nature **392**, 78-82 (1998).
[6] A. Garfinkel, Y. H. Kim, O. Voroshilovsky, Z. Qu, J. R. Kil, M. H. Lee, H. S. Karagueuzian, J. N. Weiss, and P. S. Chen, Proc. Natl. Acad. Sci. USA **97**, 6061-6066 (2000).
[7] R. A. Gray, and N. Chattipakorn, Proc. Natl. Acad. Sci. USA **102**, 4672- 4677 (2005).
[8] J. N. Weiss, P. S. Chen, Z. Qu, H. S. Karagueuzian, and A. Garfinkel, Circ. Res. **87**, 1103-1107 (2000).
[9] N. Wiener and A. Rosenblueth, Archos. Inst. Cardiol. Mex. **16**, 205-265 (1946); for another type of wave-obstacle interaction leading to spirals see: K. Agladze, J. P. Keener, S. C. Muller, and A. V. Panfilov, Science **264**, 1746-1748 (1994).
[10] M. Allessie, F. I. Bonke, and F. J. Schopman, Circ. Res. **41**, 9-18 (1977).
[11] T. Ikeda, M. Yashima, T. Uchida, D. Hough, M. C. Fishbein, W. J. Mandel, P.-S. Chen, and H. S. Karagueuzian, Circ. Res. **81**, 753-764 (1997).
[12] M. Valderrabano, Y. H. Kim, M. Yashima, T. J. Wu, H. S. Karagueuzian, and P. S. Chen, J. of Am. Coll. of Card. **36**, 2000-2008 (2000).
[13] A. M. Pertsov, J. M. Davidenko, R. Salomonsz, W. T. Baxter, and J. Jalife, Circ. Res. **72**, 631-650 (1993).
[14] Y. H. Kim, F. Xie, M. Yashima, T.-J. Wu, M. Valderrabano, M.-H. Lee, T. Ohara, O. Voroshilovsky, R. N. Doshi, M. C. Fishbein, *et al.* Circulation. **100**, 1450-1459 (1999).
[15] J. M. Davidenko, A. V. Pertsov, R. Salomonsz, W. Baxter, and J. Jalife, Nature **355**, 349-351 (1992).
[16] M. Valderrabano, P. S. Chen, and S. F. Lin, Circulation. **108**, 354-359 (2003).
[17] M. Valderrabano, M.-H. Lee, T. Ohara, A. C. Lai, M. C Fishbein, S.-F. Lin, H. S. Karagueuzian, and P. S. Chen, Circ. Res. **88**, 839-848 (2001).
[18] T.-J. Wu, J. J. Ong, C. Hwang, J. J. Lee, M. C. Fishbein, L. Czer, A. Trento, C. Blanche, R. M. Kass, W. J. Mandel, *et al.* J. of Am. Coll. of Card. **32**, 187-196 (1998).
[19] T. Ohara, K. Ohara, J.-M. Cao, M.-H. Lee, M. C. Fishbein, W. J. Mandel, P.-S. Chen, and H. S. Karagueuzian, Circulation. **103**, 1465-1472 (2001).
[20] S.-M. Hwang, T. Y. Kim, and K. J. Lee, Proc. Natl. Acad. Sci. USA **102**,10363-10368 (2005).
[21] J. M. Starobin, and C. F. Starmer, Phys. Rev. E **54**, 430 (1996).
[22] F. Xie, Z. Qu, and A. Garfinkel, Phys. Rev. E **58**, 6355-6358 (1998).
[23] A. V. Panfilov, Phys. Rev. Lett. **88**, 118101 (2002).
[24] K. H. W. J. ten Tusscher, and A.V. Panfilov, Phys. Rev. E **68**, 062902 (2003).
[25] K. H. W. J. ten Tusscher, and A.V. Panfilov, Multiscale Model. Simul. **3**, 265 (2005).
[26] S. Sinha, K. M. Stein. and D. J. Christini, Chaos **12**, 893-902 (2002).
[27] S. Takagi, A. Pumir, D. Pazo, I. Efimov, V. Nikolski, and V. Krinsky, Phys. Rev. Lett. **93**, 058101 (2004).
[28] V. N. Biktashev, and A. V. Holden, Chaos **8**, 48-56 (1998).
[29] Y.-C. Lai, and R. L. Winslow, Phys. Rev. E **50**, 3470-3474 (1994).
[30] J. C. Sommerer, and E. A. Ott, Nature **365**, 138-140 (1993).
[31] A. V. Panfilov, Chaos **8**, 57-64 (1998).

[32] A. V. Panfilov and P. Hogeweg, Phys. Lett. A **176**, 295-299 (1993).

[33] R. Pandit, A. Pande, S. Sinha, and A. Sen, Physica A **306**, 211 (2002).

[34] T. K. Shajahan, S. Sinha, and R. Pandit, Int. Journ. of Modern Physics B, **17** 5645-5654 (2003).

[35] C. H. Luo and Y. Rudy, Circ. Res. **68**, 1501-1526 (1991).

[36] T. K. Shajahan, S. Sinha, and R. Pandit, Proc. Indian Natl. Sci. Acad. **71 A**, 4757 (2005).

[37] F. H. Fenton and A. Karma, Chaos **8** 20-47 (198).

[38] F. Xie, Z. Qu, J. N. Weiss, and A. Garfinkel, Phys. Rev. E **63**, 031905 (2001).

[39] S. Sinha, A. Pande, and R. Pandit, Phys. Rev. Lett. **86**, 3678-3681 (2001).

[40] D. J. Christini and L. Glass, Chaos **12** 732-739 (2002).

[41] A. L. Hodgkin and A. F. Huxley, J.Physiol. **117**, 500-544 (1952).

[42] Z Qu, J N Weiss and A Garfinkel, Am J Physiology: Heart Circ. Physiol. **276**, H269 (1999).